

# RELATIVE COMPOSITION AND ENERGY SPECTRA OF LIGHT NUCLEI IN COSMIC RAYS: RESULTS FROM AMS-01

M. AGUILAR<sup>1</sup>, J. ALCARAZ<sup>1</sup>, J. ALLABY<sup>2,37</sup>, B. ALPAT<sup>3</sup>, G. AMBROSI<sup>3</sup>, H. ANDERHUB<sup>4</sup>, L. AO<sup>5</sup>, A. AREFIEV<sup>6</sup>, L. ARRUDA<sup>8</sup>,  
P. AZZARELLO<sup>3</sup>, M. BASILE<sup>7</sup>, F. BARAO<sup>8,9</sup>, G. BARREIRA<sup>8</sup>, A. BARTOLONI<sup>10</sup>, R. BATTISTON<sup>3,11</sup>, R. BECKER<sup>12</sup>, U. BECKER<sup>12</sup>,  
L. BELLAGAMBA<sup>7</sup>, P. BÉNÉ<sup>13</sup>, J. BERDUGO<sup>1</sup>, P. BERTUCCI<sup>3,11</sup>, B. BERTUCCI<sup>3,11</sup>, A. BILAND<sup>4</sup>, V. BINDI<sup>7</sup>, G. BOELLA<sup>14</sup>, M. BOSCHINI<sup>14</sup>,  
M. BOURQUIN<sup>13</sup>, G. BRUNI<sup>7</sup>, M. BUÉNERD<sup>15</sup>, J. D. BURGER<sup>12</sup>, W. J. BURGER<sup>11</sup>, X. D. CAI<sup>12</sup>, P. CANNARSA<sup>4</sup>, M. CAPELL<sup>12</sup>,  
D. CASADEI<sup>7</sup>, J. CASAUS<sup>1</sup>, G. CASTELLINI<sup>7,16</sup>, I. CERNUDA<sup>1</sup>, Y. H. CHANG<sup>17</sup>, H. F. CHEN<sup>18</sup>, H. S. CHEN<sup>19</sup>, Z. G. CHEN<sup>5</sup>,  
N. A. CHERNOPLEKOV<sup>20</sup>, T. H. CHIUH<sup>17</sup>, Y. Y. CHOI<sup>21</sup>, F. CINDOLO<sup>7</sup>, V. COMMICHAU<sup>22</sup>, A. CONTIN<sup>7</sup>, E. CORTINA-GIL<sup>13</sup>,  
D. CRESPO<sup>1</sup>, M. CRISTINZIANI<sup>13</sup>, T. S. DAI<sup>12</sup>, C. DELA GUIA<sup>1</sup>, C. DELGADO<sup>1</sup>, S. DI FALCO<sup>23</sup>, L. DIAMBAZOV<sup>4</sup>, I. D’ANTONE<sup>7</sup>,  
Z. R. DONG<sup>24</sup>, M. DURANTI<sup>3,11</sup>, J. ENGELBERG<sup>25</sup>, F. J. EPPLING<sup>12</sup>, T. ERONEN<sup>26</sup>, P. EXTERMANN<sup>13,37</sup>, J. FAVIER<sup>27</sup>, E. FIANDRINI<sup>3,11</sup>,  
P. H. FISHER<sup>12</sup>, G. FLÜGGE<sup>22</sup>, N. FOUQUE<sup>27</sup>, Y. GALAKTIONOV<sup>11,12</sup>, M. GERVAZI<sup>14</sup>, F. GIOVACCHINI<sup>1</sup>, P. GIUSTI<sup>7</sup>, D. GRANDI<sup>14</sup>,  
O. GRIMM<sup>4</sup>, W. Q. GU<sup>24</sup>, S. HAINO<sup>3</sup>, K. HANGARTER<sup>22</sup>, A. HASAN<sup>4</sup>, V. HERMEL<sup>27</sup>, H. HOFER<sup>4</sup>, W. HUNGERFORD<sup>4</sup>, M. IONICA<sup>11</sup>,  
M. JONGMANN<sup>4</sup>, K. KARLAMA<sup>25</sup>, W. KARPINSKI<sup>28</sup>, G. KENNEY<sup>4</sup>, D. H. KIM<sup>29</sup>, G. N. KIM<sup>29</sup>, K. S. KIM<sup>21</sup>, T. KIRN<sup>28</sup>,  
A. KLIMENTOV<sup>6,12</sup>, R. KOSSAKOWSKI<sup>27</sup>, A. KOUNINE<sup>12</sup>, V. KOUTSENKO<sup>6,12</sup>, M. KRAEBER<sup>4</sup>, G. LABORIE<sup>15</sup>, T. LAITINEN<sup>26</sup>,  
G. LAMANNA<sup>27</sup>, G. LAURENTI<sup>7</sup>, A. LEBEDEV<sup>12</sup>, C. LECHANOINE-LELUC<sup>13</sup>, M. W. LEE<sup>29</sup>, S. C. LEE<sup>30</sup>, G. LEVI<sup>7</sup>, C. H. LIN<sup>30</sup>,  
H. T. LIU<sup>19</sup>, G. LU<sup>5</sup>, Y. S. LU<sup>19</sup>, K. LÜBELSMAYER<sup>28</sup>, D. LUCKEY<sup>12</sup>, W. LUSTERMANN<sup>4</sup>, C. MAÑA<sup>1</sup>, A. MARGOTTI<sup>7</sup>, F. MAYET<sup>15</sup>,  
R. R. MCNEIL<sup>31</sup>, M. MENICHELLI<sup>3</sup>, A. MIHUL<sup>32</sup>, A. MUJUNEN<sup>25</sup>, A. OLIVA<sup>3,11</sup>, F. PALMONARI<sup>7</sup>, H. B. PARK<sup>29</sup>, W. H. PARK<sup>29</sup>,  
M. PAULUZZI<sup>3,11</sup>, F. PAUSS<sup>4</sup>, R. PEREIRA<sup>8</sup>, E. PERRIN<sup>13</sup>, A. PEVSNER<sup>33</sup>, F. PILO<sup>23</sup>, M. PIMENTA<sup>8</sup>, V. PLYASKIN<sup>6</sup>, V. POJIDAEV<sup>6</sup>,  
M. POHL<sup>13</sup>, N. PRODUIT<sup>13</sup>, L. QUADRANI<sup>7</sup>, P. G. RANCOITA<sup>14</sup>, D. RAPIN<sup>13</sup>, D. REN<sup>4</sup>, Z. REN<sup>30</sup>, M. RIBORDY<sup>13</sup>, J. P. RICHEUX<sup>13</sup>,  
E. RIIHONEN<sup>26</sup>, J. RITAKARI<sup>25</sup>, S. RO<sup>29</sup>, U. ROESER<sup>4</sup>, R. SAGDEV<sup>34</sup>, D. SANTOS<sup>15</sup>, G. SARTORELLI<sup>7</sup>, C. SBARRA<sup>7</sup>, S. SCHAEEL<sup>28</sup>,  
A. SCHULTZ VON DRATZIG<sup>28</sup>, G. SCHWERING<sup>28</sup>, E. S. SEO<sup>34</sup>, J. W. SHIN<sup>29</sup>, E. SHOUMILOV<sup>6</sup>, V. SHOUTKO<sup>12</sup>, T. SIEDENBURG<sup>12</sup>,  
R. SIEDLING<sup>28</sup>, D. SON<sup>29</sup>, T. SONG<sup>24</sup>, F. R. SPADA<sup>10</sup>, F. SPINELLA<sup>23</sup>, M. STEUER<sup>12</sup>, G. S. SUN<sup>24</sup>, H. SUTER<sup>4</sup>, X. W. TANG<sup>19</sup>,  
SAMUEL C. C. TING<sup>12</sup>, S. M. TING<sup>12</sup>, N. TOMASSETTI<sup>3,11</sup>, M. TORNIKOSKI<sup>25</sup>, J. TORSTI<sup>26</sup>, J. TRÜMPER<sup>35</sup>, J. ULBRICHT<sup>4</sup>, S. URPO<sup>25</sup>,  
E. VALTONEN<sup>26</sup>, J. VANDENHIRTZ<sup>28</sup>, E. VELIKHOV<sup>20</sup>, B. VERLAAT<sup>4,38</sup>, I. VETLITSKY<sup>6</sup>, F. VEZZU<sup>15</sup>, J. P. VIALLE<sup>27</sup>, G. VIERTTEL<sup>4</sup>,  
D. VITÉ<sup>13</sup>, H. VON GUNTEN<sup>4</sup>, S. WALDMEIER WICKI<sup>4</sup>, W. WALLRAFF<sup>28</sup>, J. Z. WANG<sup>5</sup>, K. WIK<sup>25</sup>, C. WILLIAMS<sup>7</sup>, S. X. WU<sup>12,17</sup>,  
P. C. XIA<sup>24</sup>, S. XU<sup>12</sup>, Z. Z. XU<sup>18</sup>, J. L. YAN<sup>5,37</sup>, L. G. YAN<sup>24</sup>, C. G. YANG<sup>19</sup>, J. YANG<sup>21</sup>, M. YANG<sup>19</sup>, S. W. YE<sup>18,39</sup>, H. Y. ZHANG<sup>36</sup>,  
Z. P. ZHANG<sup>18</sup>, D. X. ZHAO<sup>24</sup>, F. ZHOU<sup>12</sup>, Y. ZHOU<sup>30</sup>, G. Y. ZHU<sup>19</sup>, W. Z. ZHU<sup>5,37</sup>, H. L. ZHUANG<sup>19</sup>, A. ZICHICHI<sup>7</sup>,  
B. ZIMMERMANN<sup>4</sup>, AND P. ZUCCON<sup>3</sup>

<sup>1</sup> Centro de Investigaciones Energéticas, Medioambientales y Tecnológicas, CIEMAT, E-28040 Madrid, Spain<sup>40</sup>

<sup>2</sup> European Laboratory for Particle Physics, CERN, CH-1211 Geneva 23, Switzerland

<sup>3</sup> INFN-Sezione di Perugia, I-06100 Perugia, Italy; [nicola.tomassetti@pg.infn.it](mailto:nicola.tomassetti@pg.infn.it)

<sup>4</sup> Eidgenössische Technische Hochschule, ETH Zürich, CH-8093 Zürich, Switzerland

<sup>5</sup> Chinese Academy of Launching Vehicle Technology, CALT, 100076 Beijing, China

<sup>6</sup> Institute of Theoretical and Experimental Physics, ITEP, Moscow 117259, Russia

<sup>7</sup> University of Bologna and INFN-Sezione di Bologna, I-40126 Bologna, Italy<sup>41</sup>

<sup>8</sup> Laboratório de Instrumentação e Física Experimental de Partículas, LIP, P-1000 Lisboa, Portugal

<sup>9</sup> Instituto Superior Técnico, IST, P-1096 Lisboa, Portugal

<sup>10</sup> INFN-Sezione di Roma, I-00185 Roma, Italy<sup>41</sup>

<sup>11</sup> Università Degli Studi di Perugia, I-06100 Perugia, Italy

<sup>12</sup> Massachusetts Institute of Technology, Cambridge, MA 02139, USA

<sup>13</sup> DPNC, Université de Genève, CH-1211 GENEVA 4, Switzerland

<sup>14</sup> INFN-Sezione di Milano, I-20133 Milan, Italy<sup>41</sup>

<sup>15</sup> LPSC, Université Joseph Fourier Grenoble 1, CNRS/IN2P3, Institut Polytechnique de Grenoble, 38026 Grenoble, France

<sup>16</sup> CNR-IROE, I-50125 Florence, Italy

<sup>17</sup> National Central University, Chung-Li 32054, Taiwan

<sup>18</sup> Chinese University of Science and Technology, USTC, Hefei, Anhui 230 029, China<sup>42</sup>

<sup>19</sup> Institute of High Energy Physics (IHEP), Chinese Academy of Sciences, 100039 Beijing, China<sup>42</sup>

<sup>20</sup> Kurchatov Institute, Moscow 123182, Russia

<sup>21</sup> Ewha Womens University, 120-750 Seoul, Korea

<sup>22</sup> III. Physikalisches Institut, RWTH, D-52074 Aachen, Germany<sup>43</sup>

<sup>23</sup> INFN-Sezione di Pisa and Università di Pisa, I-56100 Pisa, Italy<sup>41</sup>

<sup>24</sup> Institute of Electrical Engineering (IEE), Chinese Academy of Sciences, 100080 Beijing, China

<sup>25</sup> Helsinki University of Technology, FIN-02540 Kytymä, Finland

<sup>26</sup> University of Turku, FIN-20014 Turku, Finland

<sup>27</sup> LAPP, Université de Savoie, CNRS/IN2P3, F-74941 Annecy-le-Vieux Cedex, France

<sup>28</sup> I. Physikalisches Institut, RWTH, D-52074 Aachen, Germany<sup>43</sup>

<sup>29</sup> CHEP, Kyungpook National University, 702-701 Daegu, Korea

<sup>30</sup> Institute of Physics, Academia Sinica, Nankang Taipei 11529, Taiwan

<sup>31</sup> Louisiana State University, Baton Rouge, LA 70803, USA

<sup>32</sup> Institute of Microtechnology, Politechnica University of Bucharest and University of Bucharest,

R-76900 Bucharest, Romania

<sup>33</sup> Johns Hopkins University, Baltimore, MD 21218, USA

<sup>34</sup> University of Maryland, College Park, MD 20742, USA

<sup>35</sup> Max-Planck Institut für extraterrestrische Physik, D-85740 Garching, Germany

<sup>36</sup> Center of Space Science and Application, Chinese Academy of Sciences, 100080 Beijing, China  
Received 2010 June 30; accepted 2010 August 23; published 2010 November 2

## ABSTRACT

Measurement of the chemical and isotopic composition of cosmic rays is essential for the precise understanding of their propagation in the galaxy. While the model parameters are mainly determined using the B/C ratio, the study of extended sets of ratios can provide stronger constraints on the propagation models. In this paper, the relative abundances of light-nuclei lithium, beryllium, boron, and carbon are presented. The secondary-to-primary ratios Li/C, Be/C, and B/C have been measured in the kinetic energy range 0.35–45 GeV nucleon<sup>-1</sup>. The isotopic ratio <sup>7</sup>Li/<sup>6</sup>Li is also determined in the magnetic rigidity interval 2.5–6.3 GV. The secondary-to-secondary ratios Li/Be, Li/B, and Be/B are also reported. These measurements are based on the data collected by the Alpha Magnetic Spectrometer AMS-01 during the STS-91 space shuttle flight in 1998 June. Our experimental results are in substantial agreement with other measurements, where they exist. We describe our light-nuclei data with a diffusive-reacceleration model. A 10%–15% overproduction of Be is found in the model predictions and can be attributed to uncertainties in the production cross-section data.

**Key words:** acceleration of particles – cosmic rays – nuclear reactions, nucleosynthesis, abundances – space vehicles

## 1. INTRODUCTION

The origin and properties of charged cosmic rays (CRs) are one of the major subjects of modern astrophysics. Though experimental information comes from the analysis of the arriving fluxes, the understanding of the relation between observational data and source properties requires a consistent picture of CR transport in the galaxy. Propagation calculations take into account the acceleration, energy losses, nuclear interactions, magnetic diffusion, and convective transport of CRs through the galactic medium (Strong et al. 2007; Maurin et al. 2001).

The propagation of CR nuclei is studied using the ratio of secondaries, which are created by the fragmentation of heavier elements, to primaries, which are produced and accelerated in astrophysical sources. The simple observation that the observed CR composition is different from that of rare solar system elements such as lithium, beryllium, and boron proves the importance of propagation in the interstellar medium (ISM) in terms of fragmentation processes. In particular, the ratio B/C between boron and its main progenitor carbon is used to constrain quantities such as the average amount of interstellar matter traversed by CRs between creation and observation, or their characteristic escape time from our galaxy. In descriptions based on diffusion theory, the secondary-to-primary ratios are mainly sensitive to the energy dependence of the diffusion coefficient  $D$ .

The light elements Li and Be are also of interest. Their abundances depend not only on interactions of the primary species C, N, and O, but also on tertiary contributions like Be→Li or B→Li. Therefore, the Li/C and Be/C ratios may provide further restrictions on propagation models (De Nolfo et al. 2006).

An accurate understanding of CR properties is also of importance in the search for exotic signals in rare components of the cosmic radiation, as the astrophysical background of any possible new physics signal must be estimated on the

basis of the existing models (Salati et al. 2010; Moskalenko et al. 2002).

The origin and evolution of the elements Li–Be–B is also a crossing point between different astrophysical fields: cosmology, astroparticle physics, and nuclear physics (Reeves 1994). The model of big bang nucleosynthesis (BBN) is able to produce only faint traces of nuclei up to  $A = 7$ . Almost all the stars consume the relatively fragile Li–Be–B nuclei in their thermonuclear core reactions. The galactic Li–Be–B are principally produced by the interaction of CRs with the ISM (Vangioni 2000). Despite many observations and proposed solutions, there are still open questions about the high value of the <sup>7</sup>Li/<sup>6</sup>Li ratio in meteorites and about the measured overabundance of primordial lithium (Asplund et al. 2006).

The CR chemical composition has been extensively studied in a wide charge and energy range both on short-duration balloon experiments (Webber et al. 1972; Orth et al. 1978; Lezniak & Webber 1978; Simon et al. 1980; Buckley et al. 1994; Hareyama & Shibata 2006) long-duration balloon flights (Ahn et al. 2008; Panov et al. 2007), and space experiments (Webber et al. 2002; Engelmann et al. 1990; Swordy et al. 1990). Isotopic composition measurements come mainly from space experiments such as the High Energy Telescopes on *Voyager 1* and 2 (Webber et al. 2002) or the Cosmic Ray Isotope Spectrometer on the *Advanced Composition Explorer* satellite (De Nolfo et al. 2003). Measurements in a wider energy range, but with poorer statistics, have been obtained by several balloon-based magnetic spectrometers (Hams et al. 2004; Ahlen et al. 2000; Webber & Kish 1979; Buffington et al. 1978). A new generation of balloon borne experiments is devoted to extending the measured range toward the knee, where the power-law decrease in the flux of CRs appears to steepen, by means of transition radiation detectors and calorimetric techniques (Ave et al. 2009; Ahn et al. 2010; Panov et al. 2007). The current and upcoming space experiments PAMELA (Orsi et al. 2007) and the Alpha Magnetic Spectrometer (AMS; Aguilar et al. 2002) rely on magnetic spectrometers, in which a magnetic field is used to bend the path of charged particles as they pass through. This allows accurate particle identification together with a precise momentum determination free from atmospheric induced backgrounds.

In this paper we present the complete analysis of our measurement of the CR charge composition and energy spec-

<sup>37</sup> Deceased.

<sup>38</sup> Now at National Institute for High Energy Physics, NIKHEF, NL-1009 DB Amsterdam, The Netherlands.

<sup>39</sup> Supported by ETH Zürich.

<sup>40</sup> Also supported by the Comisión Interministerial de Ciencia y Tecnología.

<sup>41</sup> Also supported by the Italian Space Agency.

<sup>42</sup> Supported by the National Natural Science Foundation of China.

<sup>43</sup> Supported by the Deutsches Zentrum für Luft- und Raumfahrt, DLR.

tra in the range of 0.35–45 GeV nucleon<sup>-1</sup>. Our preliminary results were presented for the B/C ratio in Tomassetti et al. (2009). The <sup>7</sup>Li-to-<sup>6</sup>Li isotopic ratio is measured in the rigidity region 2.5–6.3 GV (rigidity is defined as momentum per unit charge,  $R = pc/Ze$ ). These measurements take advantage of the large acceptance, accurate momentum resolution, and good particle identification capabilities of the AMS-01 spectrometer.

## 2. THE AMS-01 EXPERIMENT

The AMS is a particle physics detector designed for the high-precision and long-duration measurement of CRs in space. AMS-02 is scheduled to be installed on the *International Space Station* in 2010. The AMS-01 precursor experiment operated successfully during a 10 day flight on the space shuttle *Discovery* (STS-91). Data taking started on 1998 June 3. The orbital inclination was 51.7° and the geodetic altitude ranged from 320 to 390 km.

The spectrometer was composed of a cylindrical permanent magnet, a silicon microstrip tracker, time-of-flight (TOF) scintillator planes, an aerogel Čerenkov counter and anticoincidence counters (Aguilar et al. 2002). The magnet (inner diameter 1.1 m) provided a central dipole field with an analyzing power  $BL^2 = 0.14 \text{ Tm}^2$ . Six layers of a double-sided silicon microstrip tracker measured the trajectory of charged particles with an accuracy of 10  $\mu\text{m}$  in the bending coordinate and 30  $\mu\text{m}$  in the nonbending coordinate, as well as providing multiple energy-loss measurements. The TOF system had two orthogonal segmented planes at each end of the magnet, and measured the particle transit time with an accuracy of  $\sim 90$  ps for  $Z > 1$  ions. The TOF scintillators also provided energy-loss measurements up to  $|Z| = 2$ . A layer of anticoincidence scintillation counters lined the inner surface of the magnet. A thin carbon fiber layer was used as a shield to absorb low-energy particles.

A total of 100 million triggers were recorded during the mission. After the flight, the detector was calibrated with helium and carbon beams at GSI, Darmstadt, and with proton beams at the CERN PS, Geneva. The data of the precursor flight have provided significant results on galactic and trapped protons, electrons, positrons, and helium nuclei (Aguilar et al. 2002; Fiandrini et al. 2004, 2003). During the flight, nearly 200,000 nuclei with charge  $Z > 2$  were recorded by AMS-01.

## 3. DATA ANALYSIS

The physical characteristics of a detected CR particle are the arrival direction, the particle identity, and its momentum. These quantities were reconstructed combining the independent measurements provided by the various detectors. The particle rigidity was obtained by the deflection of the particle trajectory. The velocity  $\beta = v/c$  was determined from the transit time between the TOF planes along the track length. The charge magnitude  $|Z|$  was obtained by the analysis of multiple measurements of energy deposition (Section 3.2).

The response of the detector was simulated using the AMS simulation program, based on GEANT-3.21 (Brun et al. 1987) and interfaced with the hadronic package RQMD (Sorge 1995). The effects of energy loss, multiple scattering, interactions, and decays were included, as well as detector efficiency and resolution. Further details on reconstruction algorithms and detector performance are found in Aguilar et al. (2002) and references therein.

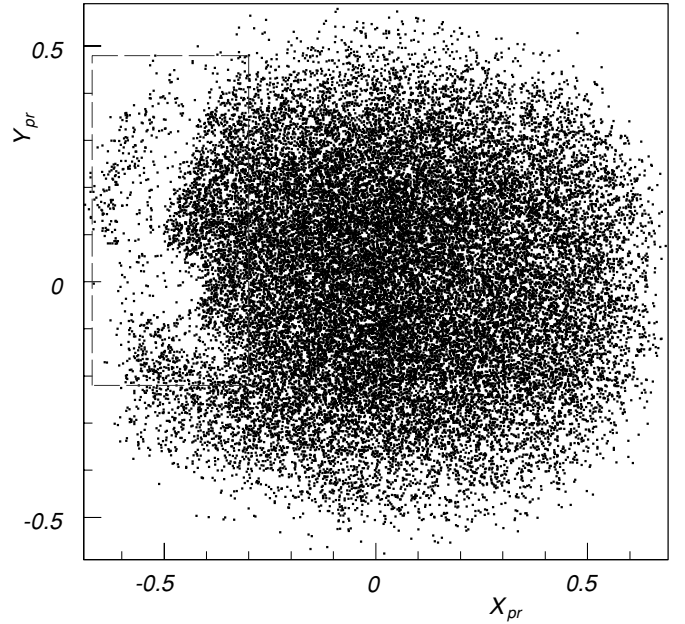


**Figure 1.** Projection plot for downward going particles with measured charges  $Z > 2$  when *Discovery* was docked with *MIR*. Note the relative deficit of events from a clearly defined region. Candidates originating from that region were removed by a geometric cut on the detector acceptance (dashed line).

During the STS-91 mission, the space shuttle *Discovery* docked with the *MIR* space station for about 4 days. The CR observations can be divided into four intervals as follows.

1. *Pre-docking*:  $\sim 1$  day of testing and checkout before docking with *MIR*.
2. *MIR-docked*:  $\sim 4$  days while the shuttle was docked with *MIR*.
3. *Post-docking*:  $\sim 3.5$  days pointing at fixed directions ( $\psi = 0^\circ, 20^\circ, 45^\circ$ ).
4. *Albedo*:  $\sim 0.5$  days pointing toward the Earth ( $\psi = 180^\circ$ ).

Here  $\psi$  is the angle between the AMS  $z$ -axis and the zenith. For the present work, we considered data collected during intervals (2) and (3). We considered only particles traversing the detector top-down within a restricted acceptance of  $32^\circ$  from the positive  $z$ -axis. Data collected while AMS-01 was passing in the region of the South Atlantic Anomaly (latitude:  $5^\circ$ – $45^\circ$ S, longitude:  $5^\circ$ – $85^\circ$ W) were excluded. For data collected during (2), a geometric cut on the detector acceptance was imposed, corresponding to *MIR*'s “shadow.” In our previous work (Aguilar et al. 2005), this region was recognized through the secondary  $\pi^\pm$  and  $\mu^\pm$  produced by primary CRs interacting with the *MIR* modules. In the nuclear channel ( $Z > 2$ ), a flux deficit can be observed in the same region. This is shown in Figure 1, where the region above AMS-01 is projected onto an  $X_{pr}$ – $Y_{pr}$  plane using the standard transformations of the arrival direction  $X_{pr} = -\sin \theta \cos \phi$  and  $Y_{pr} = \sin \theta \sin \phi$ , where  $\theta$  and  $\phi$  are the polar and azimuthal angles in the AMS coordinate system of the incoming CR nuclei. Approximately, 85,000  $Z > 2$  candidates were selected with these criteria.

### 3.1. Event Selection

In order to reject events with large nuclear scattering or poorly reconstructed trajectories, a set of quality cuts was applied to the selected candidates as follows.



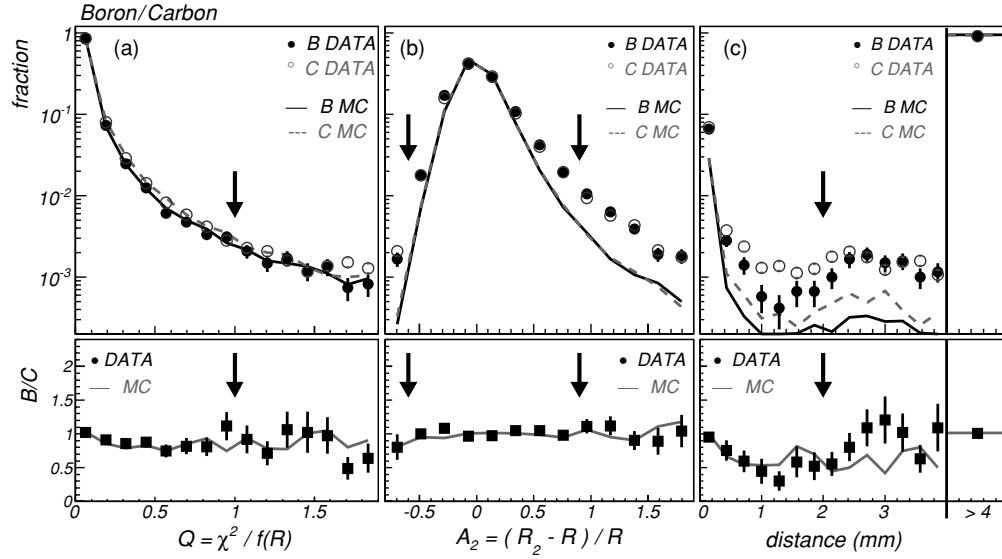


**Figure 2.** Top: normalized distributions of  $Q = \chi^2/f(R)$  (a),  $A_2$  (b), and unassociated hit distance (c) for detected boron (solid circles) and carbon (open circles) nuclei. In the cases when no hits were detected in the silicon or when the track extrapolation fell outside of the active area, the distance is set in the  $d > 4$  mm bin. The same distributions from the MC simulation data are superimposed (lines). Bottom: ratios between the corresponding distributions of B and C are shown for data (squares) and MC simulation (gray lines). Cut thresholds are described by the arrows: events are accepted (a) to the left of the arrow, (b) between the two arrows, and (c) to the right of the arrow.

1. Tracks fitted with large  $\chi^2$  were discarded according to a rigidity-dependent requirement on  $Q = \chi^2/f(R)$ , where  $R$  is the measured rigidity.
2. The particle rigidity was measured as  $R_1$  ( $R_2$ ) using the first (last) three hits along the reconstructed track. Tracks with poor agreement between  $R$ ,  $R_1$ , and  $R_2$  were removed according to cuts on  $A_1 = (R_1 - R)/R$  and  $A_2 = (R_2 - R)/R$ .
3. Consistency between  $\beta$  and  $R$  measurements was required. This cut acted on the tails of the reconstructed mass distributions of the detected particles.
4. Silicon planes with no hit associated with the track were inspected in the region around the track extrapolation. The absence of additional hits was required within a distance  $d$  of 2 mm from the track extrapolation.

As an indicator of mismeasured particles, a fraction of  $\sim 4\%$  of events with negative measured rigidity ( $R < 0$ ) was found in the reconstructed data before applying the selection cuts. These events were used as a control sample to define the selection. The total selection efficiency was found to be substantially charge independent over the whole energy range considered. In Figure 2, the distributions of some quantities that were used for the selection are shown for boron and carbon in comparison with the Monte Carlo (MC) simulation. The agreement between data and MC simulation in general is good; in the tails of the distributions, especially  $A_2$ , the MC simulation is less accurate in describing the measured behavior (some few percent of the sample). However, these features have similar magnitudes for the considered species and on average cancel out in the ratio, as shown in the lower panels of the figure. Similar conclusions can be drawn for the ratios Li/C and Be/C.

### 3.2. Particle Identification

Each elemental species is identified by its charge  $Z$ . The dynamical response of the TOF scintillators allowed particle discrimination up to  $Z = 2$ . The analysis of particle charge for  $Z > 2$  events was performed by the study of the energy

losses recorded in the silicon layers. The ionization energy generated by a charged particle in a silicon microstrip detector was collected as a cluster of adjacent strips. Tracker clusters were recognized online and then reprocessed with the reconstruction software. A multistep procedure of normalization of the cluster signals was performed (Tomassetti 2009). The method accounted for saturation effects, electronics response, particle inclination, and velocity dependence of the energy loss. The charge identification algorithm, applied to the corrected signals, was based on the maximum likelihood method which determines the most likely value of  $Z$  corresponding to the maximum value of the log-likelihood function:

$$L(Z) = \log_{10} \left\{ \prod_{k=1}^{k=6} P_Z^k(x_k, \beta) \right\}. \quad (1)$$

The  $k$ -index refers to the six silicon layers,  $x_k$  are the corrected cluster signals as observed in the  $k$ th layer. The normalized  $P_Z^k(x_k, \beta)$  functions are the probabilities of a given charge  $Z$  with velocity  $\beta$  to produce a signal  $x_k$  in the  $k$ th layer. These probability density functions were estimated with a high-purity reference sample of flight data, and describe the energy-loss distributions  $x_k$  around a mean value  $\mu_{Z,\beta} \propto (Z^2/\beta^2) \log(\gamma)$  as expected by the Bethe–Bloch formula. This  $\beta$ – $Z$  dependence is shown in Figure 3 for  $Z = 3$ –8 (dashed lines) superimposed on the mean energy deposition from the measured tracker signals. Due to inefficiencies in charge collection, some energy losses may produce charge responses which do not carry reliable information on the particle charge. For this reason, not all the six clusters were used to determine  $Z$ . For each reconstructed track, the most reliable set of three clusters  $\Omega = \{k_1, k_2, k_3\}$  was selected by also using  $\Omega$  as a parameter of log likelihood function:

$$L(Z, \Omega) = \log_{10} \{ P_Z^{k_1} \cdot P_Z^{k_2} \cdot P_Z^{k_3} \}, \quad (2)$$

where the free parameters to be determined are  $Z$ , ranging from 3 (lithium) to 8 (oxygen), and  $\Omega$ , running over all the three-fold combinations  $\{k_1, k_2, k_3\}$  of the tracker signals. Though the

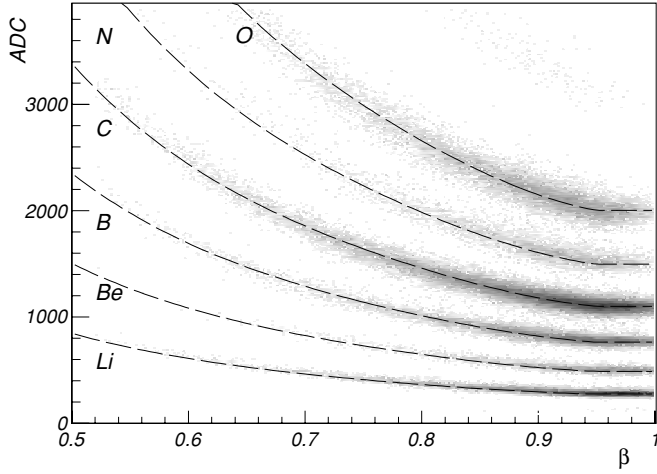


**Figure 3.** Mean energy loss in the silicon tracker as a function of the measured velocity  $\beta$ . The signal amplitude, shown in ADC count units, is the average signal of the best clusters  $\{k_1, k_2, k_3\}$ . Different nuclear species fall into distinct charge bands. The  $\beta$ - $Z$  dependence of  $\mu_{Z,\beta}$  is superimposed for  $Z = 3$  to  $Z = 8$  (dashed lines).

final estimation of  $Z$  was provided by three tracker clusters, all the selected clusters were processed in Equation (2). An identification inefficiency of a few percent was achieved with this algorithm. On the basis of the final charge spectrum shown in Figure 4, the determination of B and C was done with a charge resolution better than 0.14 charge units.

### 3.3. Charge Contamination

The charge assignment procedure was studied in terms of efficiency and contamination. Each nucleus of charge  $3 \leq Z \leq 8$  produces a charge estimation  $\hat{Z}$  which can be related to its true impinging charge  $Z$  by using a set of coefficients  $F_Z^{\hat{Z}}$ .

The  $6 \times 6$  matrix  $\|F\|$  is diagonally dominated, and each off-diagonal element  $F_Z^{\hat{Z}}$  represents the probability of a nuclear species  $Z$  to be misidentified as  $\hat{Z}$  due to interactions in the detector material and fluctuations of the energy loss:

$$F_Z^{\hat{Z}} = P(\hat{Z}|Z). \quad (3)$$

Two different contributions produce a charge migration  $Z \rightarrow \hat{Z}$ .

1. After interacting in the upper TOF material, an incoming nucleus  $Z$  may fragment and physically turn into  $\hat{Z}$ . These events were typically rejected by the anticoincidence veto. However, a fraction of them produces a clean track in the tracker, passing trigger and selection. Since  $\hat{Z} < Z$ , the corresponding matrix is triangular.
2. Fluctuations of the measured energy loss produce a nonzero  $Z \rightarrow \hat{Z}$  migration probability. This charge spillover is typically symmetric and in most cases comes from adjacent charges, i.e.,  $\hat{Z} = Z \pm 1$ .

Both the effects were studied with MC simulations. The second contribution was also estimated with the data. Possible charge migrations from/to the  $Z < 3$  and  $Z > 8$  species were also considered, in particular to achieve a suitable separation of the  $Z > 2$  candidates from the background of the more abundant helium flux. Helium–lithium separation was performed with the combination of both TOF and tracker energy depositions and studied with the help of data from the calibration beam test during which the detector was probed with pure helium

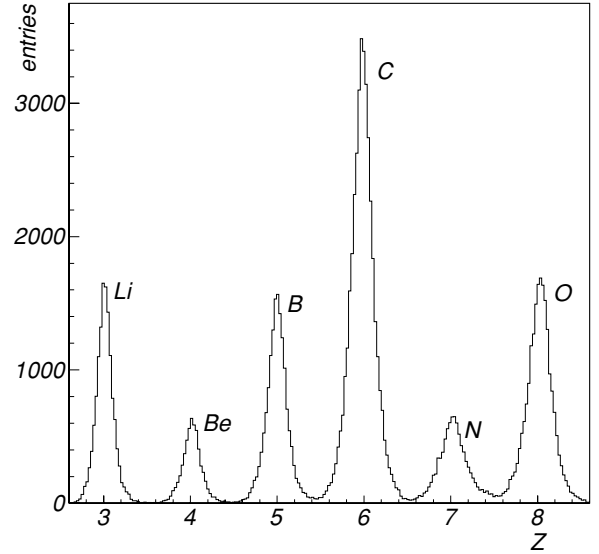


**Figure 4.** Charge spectrum of the selected  $Z > 2$  data. The signal amplitudes of Figure 3 are equalized to  $\beta \equiv 1$  and shown in units of charge. Different nuclear species fall in distinct charge peaks.

beams at 0.75, 1.8, 3.6, and 8 GeV nucleon<sup>-1</sup> of kinetic energy (Aguilar et al. 2002). Contamination from He to the selected  $Z > 2$  sample was estimated to be less than  $10^{-4}$  of the helium sample. The effects of charge misassignment in the measured secondary-to-primary ratios turned out to be smaller than the statistical uncertainties; this effect is included in the systematic errors (Section 4.3).

## 4. FLUX DETERMINATION

Before the secondary-to-primary ratios can be determined, the spectra must be transformed into fluxes  $\Phi$ . The differential energy spectrum of the  $Z$ -charged particles measured by AMS-01 in the energy bin  $E$  of width  $\Delta E$  is related to the measured counts  $\Delta N^Z$  by

$$\Phi^Z(E) = \frac{\Delta N^Z(E)}{A^Z(E) \cdot \Delta T^Z(E) \cdot \Delta E}, \quad (4)$$

where  $\Delta T^Z(E)$  is the effective exposure time (Section 4.1) and  $A^Z(E)$  is the detector acceptance (Section 4.2). The relation between the measured energy of detected particles and their true energy was studied using unfolding techniques (D'Agostini 1995). Making use of an appropriate energy binning, the final smearing effects turned out to be barely appreciable and very similar for the various species, i.e., the overall effect is mostly canceled out in the bin-to-bin ratios. The rigidity resolution curve of AMS-01 is shown in Figure 5 for carbon nuclei measured during the flight and in the beam test, together with the simulation results.

### 4.1. Exposure Time

By the term exposure time  $\Delta T^Z(E)$ , we mean the effective data taking duration with AMS-01 capable of receiving a new trigger from a galactic particle of charge  $Z$  in the energy interval  $\Delta E$ . The detection is influenced by the trigger livetime fraction  $\alpha$  and the geomagnetic field modulation. Though no atmospheric or trapped particles are expected in our  $Z > 2$  fluxes, the position-dependent geomagnetic cutoff introduces different distortions of the measured energy spectrum for

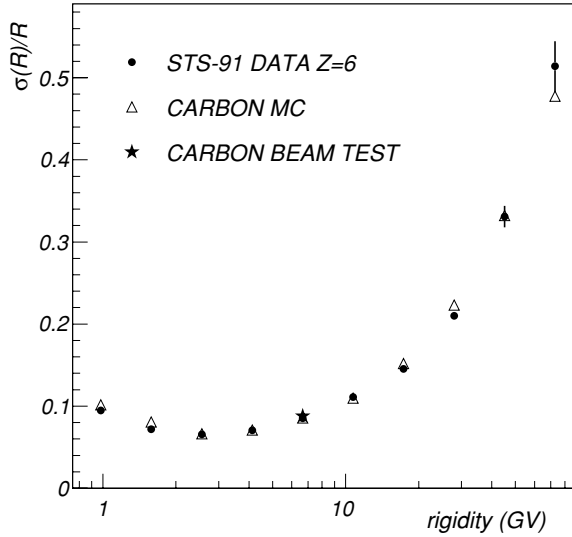


**Figure 5.** Rigidity resolution of the AMS-01 silicon tracker estimated with the measured data from the flight and the calibration test beam with carbon nuclei in comparison with the MC simulation.

different nuclear species. Hence, only particles with rigidity greater than  $R^{\text{Th}} = 1.25 \cdot R_C$  were accepted, where  $R_C$  is the rigidity cutoff obtained from the Störmer estimation in the corrected geomagnetic coordinates for 1998 (Smart & Shea 2005). The entire orbit was divided into 45,000 time intervals of  $\delta t \sim 10$  s. For each time bin  $\delta t_k$ , the mean values of  $R_k^{\text{Th}}$  and  $\alpha_k$  (trigger livetime fraction) were computed. The exposure time  $\Delta T^Z(E)$  was then calculated for each particle  $Z$ , rigidity  $R$ , and energy  $E \in \Delta E$  as

$$\Delta T^Z(E) = \sum_k \alpha_k \cdot H_k^Z(R, R_k^{\text{Th}}) \cdot \delta t_k, \quad (5)$$

where  $R = \left(\frac{A}{Z}\right) \sqrt{E^2 + 2M_p E}$ ,  $H = 1$  for  $R > R^{\text{Th}}$ , and  $H = 0$  for  $R < R^{\text{Th}}$ , i.e., the sum is restricted to only the time intervals above cutoff. The result describes the effective exposure of AMS-01 to CRs in that energy bin coming from outside the magnetosphere. Note that  $\Delta T^Z(E)$  as a function of the kinetic energy per nucleon is different for different  $A/Z$  isotopes; since  $A/Z$  is slightly different for the elements under consideration, their corresponding exposure times do not completely cancel in the flux ratios.

#### 4.2. Acceptance Estimation

The detector acceptance  $A^Z(E)$  of Equation (4) is the convolution of geometrical factors with the energy-dependent efficiency  $\epsilon$ , including trigger, reconstruction, and selection efficiencies. The acceptances of each species  $A^Z$  were determined with the MC simulation (Sullivan 1971).  $2 \times 10^8$  trajectories were generated in the energy range 0.2–50 GeV nucleon<sup>-1</sup>, according to an isotropic distribution and a power-law momentum distribution  $\propto p^{-1}$ . The recorded MC simulation events were sent through the same analysis chain as for the measured data. Background fluxes were also simulated, up to  $Z = 8$ .

#### 4.3. Systematic Errors

Though systematic uncertainties arising from many steps of the analysis are suppressed in the ratios, differences in the trigger efficiencies of the two species are present, as expected, from the charge dependence of delta ray production and fragmentation effects in the detector material. The spillover from adjacent charges also produces net effects on the measurements.

The MC simulation determination of the acceptance gave a statistical uncertainty of  $\sim 1\%$ – $4\%$ , increasing with energy.  $A^Z(E)$  decreases with increasing energy and charge, due to the trigger conditions against interacting particles. In the events collected from the flight, the dedicated unbiased data set<sup>44</sup> did not give enough statistics for an energy-dependent validation of the  $Z > 2$  trigger efficiency with the measured data; hence, this estimation must rely on simulation results. Since CR interactions with the detector material can play an important role in the observed behavior of the trigger response, a GEANT3-based MC simulation does not guarantee a model-independent description of the experimental setup. Therefore, this study was performed with three different models. A Virtual MC application (Hrivnacova et al. 2003) was developed for AMS-01. The simulation natively supports the particle transport codes GEANT3 and GEANT4 (Agostinelli et al. 2003). An additional interface with FLUKA (Fassò et al. 2005) was developed (Oliva 2007; Tomassetti 2009). Since the quantities that enter into our measurements are the ratios  $\eta_T$  between the corresponding acceptances  $A^{\text{Li}}/A^{\text{C}}$ ,  $A^{\text{Be}}/A^{\text{C}}$ , and  $A^{\text{B}}/A^{\text{C}}$ , the systematic errors on the trigger efficiency were estimated observing the scatter between the three different models. Results of this approach are summarized in Figure 6. From the figure the charge-dependent behavior of the trigger response is clear; the energy dependence of the trigger efficiency is more pronounced

<sup>44</sup> One out of 1000 events was recorded with the AMS-01 unbiased trigger.

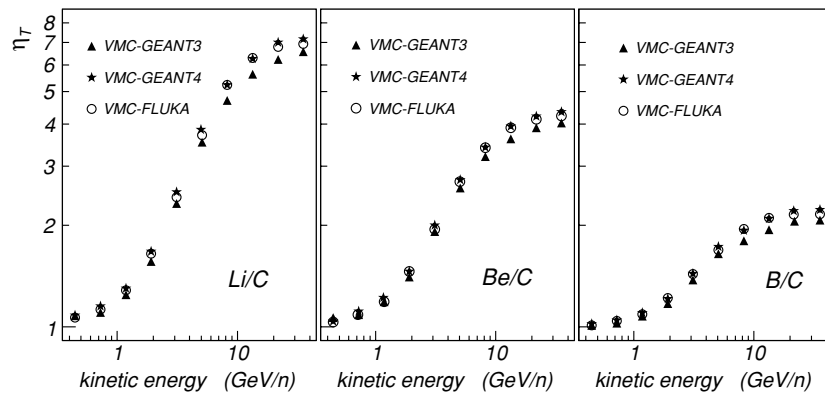


**Figure 6.** Ratio of acceptances  $\eta_T$  estimated with GEANT3-, GEANT4-, and FLUKA-based simulations implemented under the AMS-VMC application.

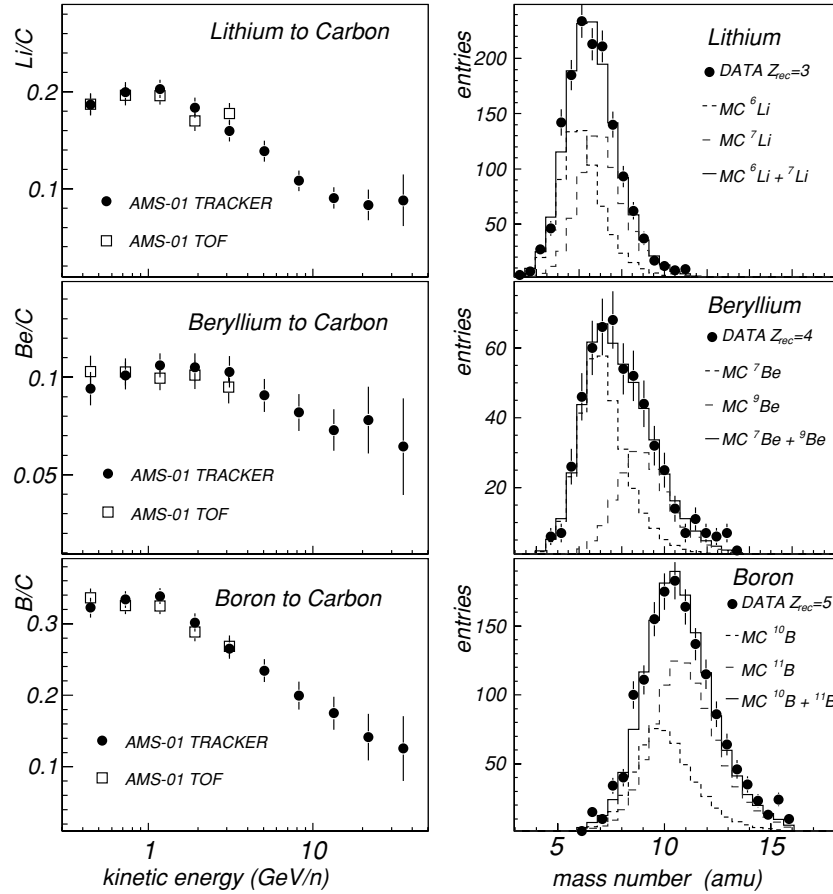


**Figure 7.** Left: consistency check of the Li/C, Be/C, and B/C ratios obtained with tracker measurements between 0.35 and 45 GeV nucleon<sup>-1</sup> (filled circles) in comparison with that measured with the TOF between 0.35 and 4 GeV nucleon<sup>-1</sup> (open squares). Error bars include both statistical and systematic errors. Right: mass number distribution of measured (filled circles) and simulated (lines) isotopes for  $\beta < 0.95$ . MC simulation curves are normalized to the data and contain isotopic mixtures of  ${}^6\text{Li}$ – ${}^7\text{Li}$ ,  ${}^9\text{Be}$ – ${}^7\text{Be}$ , and  ${}^{10}\text{B}$ – ${}^{11}\text{B}$ .

for higher charges. Good agreement was found between GEANT4 and FLUKA; nevertheless, for each ratio, the full envelope of the three model curves was considered as the uncertainty band of the trigger efficiency.

Another source of uncertainty comes from the isotopic composition of the measured nuclei. In order to compute bin-to-bin ratios, all the elemental fluxes were determined in a common grid of kinetic energy per nucleon  $E$ . The rigidity to energy conversion required the  $A/Z$  ratio of each charged species. To first approximation  $A/Z \approx 2$  for the light  $Z > 2$  nuclei under study; however, according to existing measurements and model calculations, more realistic isotopic mixtures can be considered for the Li–Be–B group (Hams et al. 2004; Ahlen et al. 2000; Webber et al. 2002; Buffington et al. 1978). Hence, we assumed isotopic fractions  ${}^6\text{Li}/({}^6\text{Li} + {}^7\text{Li}) = 0.5 \pm 0.15$ ,  ${}^7\text{Be}/({}^7\text{Be} + {}^9\text{Be}) = 0.65 \pm 0.15$ , and  ${}^{10}\text{B}/({}^{10}\text{B} + {}^{11}\text{B}) = 0.35 \pm 0.15$ , accounting for these uncertainties in the estimation of the systematic error. In the left panels of Figure 7, we cross-checked our measured ratios with independent measurements obtained with the TOF system, which provided a direct measurement of the velocity and hence kinetic energy per nucleon. Results from the tracker measurement and the TOF measurement are consistent. The right panels of Figure 7 show the reconstructed mass distributions for the Li–Be–B events above cutoff with  $\beta < 0.95$ . Though the AMS-01 mass resolution did not allow an event-to-event isotopic separation, the data are in good agreement with the MC simulation which contains the assumed mixtures.

A detailed summary of the uncertainties on the measured ratios Li/C, Be/C, and B/C is presented in terms of relative errors in Figure 8. The sources of uncertainties taken into account are the statistics of collected events, MC simulation statistics, contamination due to charge misidentification (Section 3.3), uncertainty on isotopic composition, and trigger efficiency uncertainty.

## 5. RESULTS AND DISCUSSION

### 5.1. The ${}^7\text{Li}/{}^6\text{Li}$ Isotopic Ratio

A composition fit technique for determining the isotopic ratio  ${}^7\text{Li}/{}^6\text{Li}$  in four rigidity intervals between 2.5 and 6.3 GV was performed (Zhou 2009). The best fits were obtained by leaving the amplitudes for both isotopes free in all four rigidity intervals as shown in Figure 9. The fits gave unique minima for the  ${}^7\text{Li}/{}^6\text{Li}$  ratios in each rigidity region, providing an average ratio of  $1.07 \pm 0.16$  in the region 2.5–6.3 GV. The results are shown in Figure 10 with the previous experimental data (De Nolfo et al. 2003; Webber et al. 2002; Hams et al. 2004; Ahlen et al. 2000; Webber & Kish 1979; Buffington et al. 1978); the latter are converted into units of rigidity, allowing a direct comparison with our data. Point values are listed in Table 1. Our measurement agrees with the previous data and extends to higher energies. In summary, our new measurements of  ${}^7\text{Li}/{}^6\text{Li}$  extends to 6.3 GV of rigidity ( $\sim 2$  GeV nucleon<sup>-1</sup> of kinetic energy) with a constant ratio of about equal abundance of both isotopes.

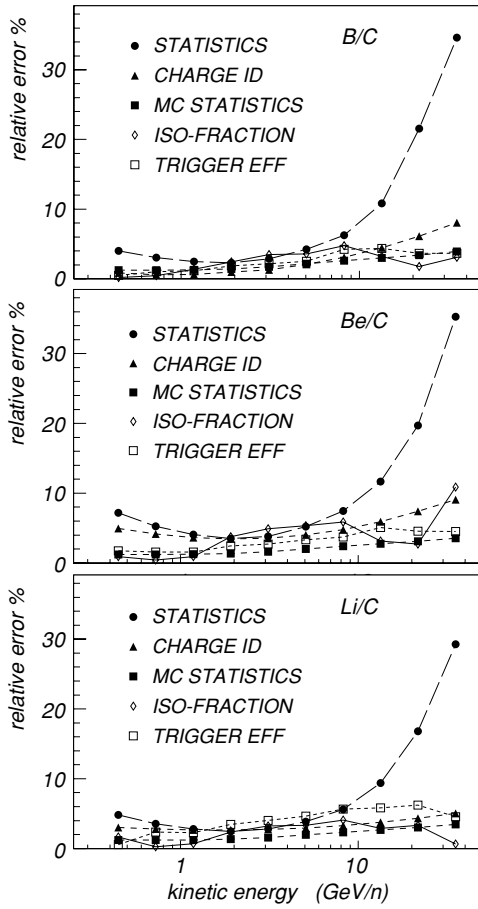


**Figure 8.** Relative errors on the measured ratios Li/C, Be/C, and B/C. The contributions from data statistics, MC statistics, contamination on the charge identification, isotopic composition, and trigger efficiency are shown as a function of the kinetic energy per nucleon. For the sake of graphical clarity, points are connected with lines.

### 5.2. Secondary-to-Primary Ratios

Results for the Li/C, Be/C, and B/C ratios are presented in Figure 11 with the existing experimental data (Webber et al. 1972; Orth et al. 1978; Lezniak & Webber 1978; Engelmann et al. 1990; Ahn et al. 2008; De Nolfo et al. 2003).

The energy range  $0.35\text{--}45\text{ GeV nucleon}^{-1}$  is limited by selection inefficiencies below  $\sim 0.35\text{ GeV nucleon}^{-1}$  and the lack of statistics above  $45\text{ GeV nucleon}^{-1}$ . The error bars in the figure represent the sum in quadrature of statistical errors with the systematic uncertainties. These results are summarized in Table 2.

Our B/C ratio measurement agrees well with the results from the first flight of CREAM in 2004 (Ahn et al. 2008) and with the data collected by HEAO-3-C2 (Engelmann et al. 1990) from 1979 October and 1980 June. The Be/C ratio is consistent, within errors, with the HEAO data, but not with balloon data Orth et al. (1978). Our Li/C data have unprecedented accuracy in a poorly explored energy region. In comparison with balloon data from Orth et al. (1978), our data indicate a quite different trend in the high-energy part of the Li/C ratio.

In these ratios, the main progenitors of boron nuclei are primary CRs (CNO). In contrast, the abundances of Li and Be also depend on secondary progenitors Be and B through tertiary contributions such as  $B \rightarrow Be$ ,  $Be \rightarrow Li$ , and  $B \rightarrow Li$ .

However, the observed shapes of the measured ratios Li/C and Be/C suggest their suitability in constraining the propagation parameters: their decreasing behavior with increasing energy is a direct consequence of the magnetic diffusion experienced by their progenitors, while the characteristic peak around  $\sim 1\text{ GeV nucleon}^{-1}$  is a strong indicator of low-energy phenomena like stochastic reacceleration or convective transport with the galactic wind.

### 5.3. Secondary to Secondary Ratios

For the sake of completeness, in Figure 12 and Table 3 we report the secondary-to-secondary ratios Li/Be, Li/B, and Be/B. Though their values can be derived from the secondary-

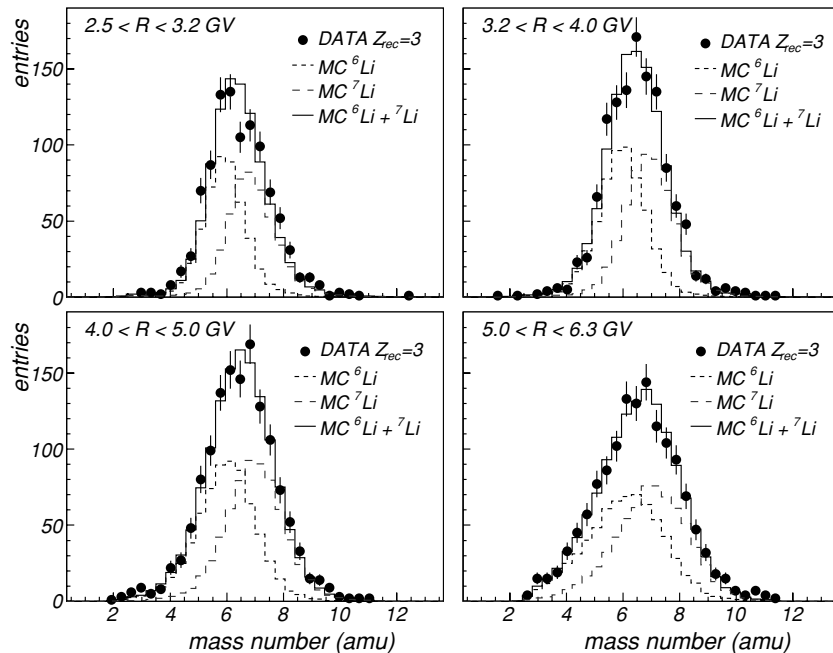


**Figure 9.** Lithium mass distributions and best-fitting composition in four rigidity regions. The amplitudes of the simulated distribution of  ${}^7\text{Li}$  and  ${}^6\text{Li}$  are free parameters.



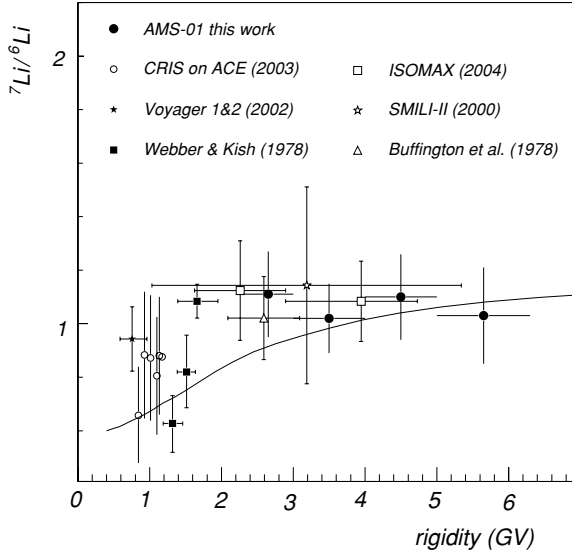


**Figure 10.** Rigidity dependence of the ratio  ${}^7\text{Li}/{}^6\text{Li}$ . The other experimental values are converted from kinetic energy to rigidity. The solid line is a diffusion model prediction using GALPROP (Section 5.4).

**Table 1**  
The Isotopic Ratio  ${}^7\text{Li}/{}^6\text{Li}$

Rigidity (GV)	2.5–3.2	3.2–4.0	4.0–5.0	5.0–6.3
${}^7\text{Li}/{}^6\text{Li}$	$1.11 \pm 0.16$	$1.02 \pm 0.13$	$1.10 \pm 0.16$	$1.03 \pm 0.18$
$\chi^2/\text{d.f.}$	35.1/35	46.1/39	41.2/43	42.6/43

to-primary ratios of Table 2, a dedicated analysis of uncertainty was done for these channels. These quantities are less sensitive to the propagation parameters because all the secondaries have the same origin and undergo similar astrophysical processes. These ratios are also found to be less influenced by solar modulation. Hence, these relative abundances maximize the effects of the nuclear aspects of the CR propagation: decays, fragmentations, and catastrophic losses. As pointed out in Webber & Soutoul (1998), the Be/B ratio is sensitive to the radioactive decay of the beryllium (numerator) which enriches the boron flux (denominator); thus, a precise measurement of the Be/B ratio provides constraints on the galactic halo size as well as the  ${}^{10}\text{Be}/{}^9\text{Be}$  ratio. The observed increasing behavior of the Be/B ratio is due to the relativistic lifetime dilation of the unstable Be. However, the migration  ${}^{10}\text{Be} \rightarrow {}^{10}\text{B}$  involves only a small fraction of the elemental flux, and the present data are still affected by sizeable errors.

#### 5.4. Propagation Calculations

To describe our results, we made use of GALPROP v50.1p,<sup>45</sup> a numerical code that incorporates all the astrophysical inputs of the CR galactic transport (Strong & Moskalenko 1998). We described the propagation in the framework of the diffusive-reacceleration model, which has been very successful in the description of the CR nuclei fluxes (Moskalenko et al. 2002). GALPROP solves the diffusion transport equation for a given source distribution and boundary conditions for all the galactic CRs. In this model, the magnetic diffusion is described in terms of a rigidity-dependent diffusion coefficient  $D = \beta D_0 (R/R_0)^\delta$ . The magnitude of the diffusion, related to the level of hydromagnetic turbulence, is controlled by the parameter  $D_0$  which fixes the normalization of  $D(R)$  at the reference rigidity  $R_0$ . The spectral index  $\delta$  is linked to the density of the magnetic irregularities at small scales. Reacceleration is an energy gain of charged particles due to scattering on hydromagnetic waves moving at Alfvén speed  $V_a$  in the ISM. This process is described as a diffusion in the momentum space and controlled by the parameter  $V_a$ . The source spectra  $q(R)$  are assumed to have a pure power-law dependence in rigidity, i.e.,  $q(R) \propto R^{-\alpha}$ . The boundary conditions are expressed by imposing free escape at the galactic halo boundaries, in particular by the halo height  $H$ . Energy losses and catastrophic losses over the ISM are included. The code makes use of an up-to-date nuclear reaction network, including decay rates and fragmentation cross sections for all the relevant channels. Semi-empirical models for cross section calculations are tuned with the measured data, where available (Moskalenko & Mashnik 2003). Equilibrium solutions are provided for the local interstellar spectra (LIS) of all the galactic CRs. In our description, we used a 2D cylindrically symmetric model of the galaxy. For the heliospheric propagated fluxes, we adopted the force field description of the solar wind (Gleeson & Axford 1968). We used  $\phi = 450$  MV as the modulation parameter, consistent with 1998 June (Wiedenbeck et al. 2007). The parameter values of our GALPROP settings are listed in Table 4.

In Figures 11 and 12, our data are compared with the model calculation in the heliosphere (solid lines). The LIS ratios (dashed lines) are shown for reference. Our results for the B/C ratio, the Li/C ratio, and the  ${}^7\text{Li}/{}^6\text{Li}$  isotopic fraction of Figure 10 are described quite well within the uncertainties. It is difficult, however, to accommodate the Li and B description with the Be/C ratio by means of only astrophysical parameters. Beryllium appears to be overproduced in the model by a factor of

<sup>45</sup> <http://galprop.stanford.edu>

**Table 2**  
The Secondary to Primary Ratios of Li/C, Be/C, and B/C Between Kinetic Energies of 0.35 and 45 GeV nucleon<sup>-1</sup>

$\Delta E$	$\langle E \rangle^a$	Li/C	STAT	SYS	Be/C	STAT	SYS	B/C	STAT	SYS
0.35–0.57	0.45	0.187	$\pm 0.009$	$\pm 0.007$	0.094	$\pm 0.007$	$\pm 0.005$	0.323	$\pm 0.013$	$\pm 0.005$
0.57–0.92	0.73	0.200	$\pm 0.007$	$\pm 0.008$	0.101	$\pm 0.005$	$\pm 0.005$	0.334	$\pm 0.010$	$\pm 0.006$
0.92–1.50	1.18	0.203	$\pm 0.006$	$\pm 0.008$	0.106	$\pm 0.004$	$\pm 0.004$	0.339	$\pm 0.008$	$\pm 0.008$
1.50–2.44	1.92	0.184	$\pm 0.004$	$\pm 0.009$	0.105	$\pm 0.004$	$\pm 0.006$	0.302	$\pm 0.007$	$\pm 0.011$
2.44–3.97	3.11	0.159	$\pm 0.004$	$\pm 0.010$	0.103	$\pm 0.004$	$\pm 0.007$	0.265	$\pm 0.008$	$\pm 0.012$
3.97–6.45	5.06	0.139	$\pm 0.005$	$\pm 0.009$	0.091	$\pm 0.005$	$\pm 0.007$	0.234	$\pm 0.010$	$\pm 0.012$
6.45–10.5	8.22	0.108	$\pm 0.006$	$\pm 0.009$	0.082	$\pm 0.006$	$\pm 0.007$	0.199	$\pm 0.012$	$\pm 0.015$
10.5–17.0	13.36	0.090	$\pm 0.008$	$\pm 0.007$	0.073	$\pm 0.009$	$\pm 0.006$	0.175	$\pm 0.019$	$\pm 0.013$
17.0–27.7	21.72	0.083	$\pm 0.014$	$\pm 0.007$	0.078	$\pm 0.015$	$\pm 0.008$	0.141	$\pm 0.030$	$\pm 0.011$
27.7–45.0	35.30	0.088	$\pm 0.026$	$\pm 0.007$	0.064	$\pm 0.023$	$\pm 0.010$	0.126	$\pm 0.043$	$\pm 0.013$

**Notes.** The columns indicate: energy intervals  $E_1$ – $E_2$ , reference values  $\langle E \rangle$ , measured ratios, statistical errors, and systematic errors.

<sup>a</sup> The reference energy  $\langle E \rangle$  is computed as the geometric mean  $\sqrt{E_1 E_2}$ .

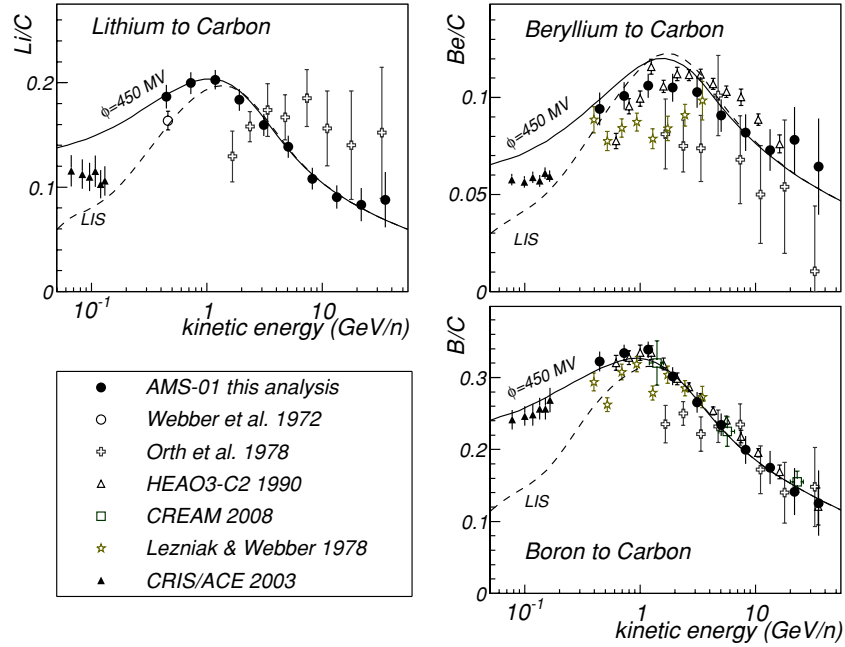


**Figure 11.** Results for the secondary-to-primary ratios Li/C, Be/C, and B/C from this work (solid circles) and previous measurements (Webber et al. 1972; Orth et al. 1978; Lezniak & Webber 1978; Engelmann et al. 1990; Ahn et al. 2008; De Nolfo et al. 2003). Model calculations are also reported, from the GALPROP diffusive-reacceleration model predictions for interstellar (LIS) and solar modulated ( $\phi = 450$  MV) CR fluxes (Strong & Moskalenko 1998).

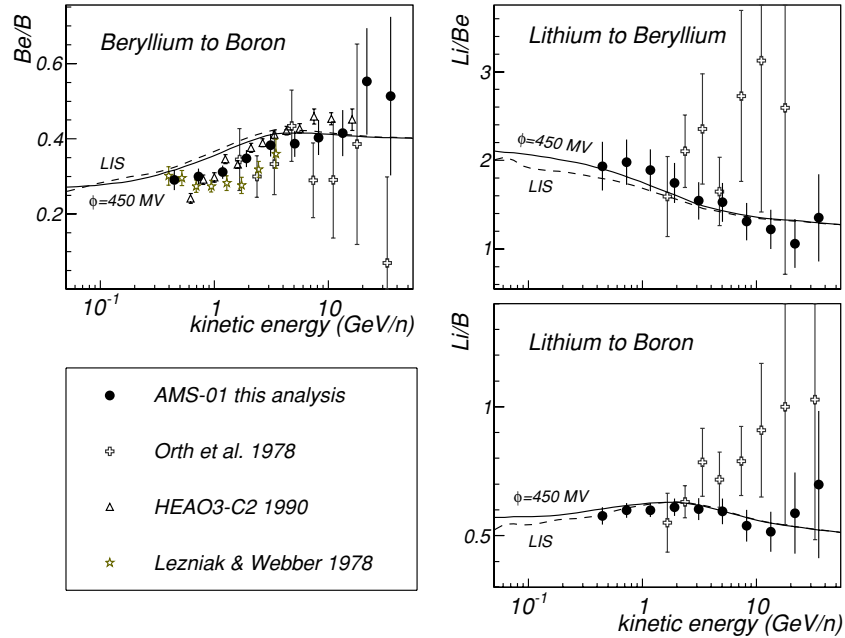


**Figure 12.** Secondary-to-secondary ratios Be/B, Li/Be, and Li/B from this work (solid circles) and previous measurements (Orth et al. 1978; Lezniak & Webber 1978; Engelmann et al. 1990). Model calculations are also reported, from the GALPROP diffusive-reacceleration model predictions for interstellar (LIS) and solar modulated ( $\phi = 450$  MV) CR fluxes (Strong & Moskalenko 1998).

$\sim 10\%$ – $15\%$ . This discrepancy is also apparent in the previous measurements. The ratios Be/B and Li/Be in Figure 12 also indicate this feature, whereas the Li/B ratio is well described by our GALPROP tune.

It is worth noting that the production of Li and Be involves very complex reaction chains due to the multichannel character of the CR fragmentation. Moreover, cross sections for the tertiary processes  $\text{LiBeB} + \text{ISM} \rightarrow \text{LiBe}$  are less well known than for the interactions  $\text{CNO} + \text{ISM} \rightarrow \text{LiBeB}$ . Spallation contribu-

tions like  $^{11}\text{B} \rightarrow ^9\text{Be}$  are measured at only a few energy points. Other channels such as  $^{10}\text{B} \rightarrow ^9\text{Be}$ ,  $^{14,15}\text{N} \rightarrow ^9\text{Be}$  or  $^{10,11}\text{B} \rightarrow ^7\text{Be}$  are not measured at all and rely on extrapolated parameterizations (Moskalenko & Mashnik 2003). Spallation processes involving interstellar helium are even less well understood. The lack of cross section measurements limits the model predictions to uncertainties of  $\sim 10\%$ – $20\%$  in the Li/C and Be/C ratios (De Nolfo et al. 2006). Understanding fragmentation is a key factor in establishing final conclusions concerning CR propagation.

**Table 3**  
Secondary-to-Secondary Ratios of Li/Be, Li/B, and Be/B Between Kinetic Energies of 0.35 and 45 GeV nucleon<sup>-1</sup>

$\Delta E$	$\langle E \rangle^a$	Li/Be	STAT	SYS	Li/B	STAT	SYS	Be/B	STAT	SYS
0.35–0.57	0.45	1.935	$\pm 0.157$	$\pm 0.225$	0.577	$\pm 0.030$	$\pm 0.015$	0.291	$\pm 0.023$	$\pm 0.014$
0.57–0.92	0.73	1.979	$\pm 0.118$	$\pm 0.227$	0.598	$\pm 0.024$	$\pm 0.014$	0.300	$\pm 0.017$	$\pm 0.012$
0.92–1.50	1.18	1.889	$\pm 0.085$	$\pm 0.221$	0.599	$\pm 0.020$	$\pm 0.017$	0.311	$\pm 0.013$	$\pm 0.012$
1.50–2.44	1.92	1.747	$\pm 0.066$	$\pm 0.216$	0.610	$\pm 0.020$	$\pm 0.027$	0.348	$\pm 0.013$	$\pm 0.019$
2.44–3.97	3.11	1.544	$\pm 0.065$	$\pm 0.202$	0.603	$\pm 0.024$	$\pm 0.035$	0.384	$\pm 0.015$	$\pm 0.026$
3.97–6.45	5.06	1.528	$\pm 0.084$	$\pm 0.203$	0.594	$\pm 0.032$	$\pm 0.037$	0.387	$\pm 0.022$	$\pm 0.027$
6.45–10.5	8.22	1.310	$\pm 0.105$	$\pm 0.183$	0.539	$\pm 0.045$	$\pm 0.042$	0.404	$\pm 0.033$	$\pm 0.033$
10.5–17.0	13.36	1.223	$\pm 0.157$	$\pm 0.155$	0.515	$\pm 0.069$	$\pm 0.036$	0.416	$\pm 0.057$	$\pm 0.022$
17.0–27.7	21.72	1.062	$\pm 0.238$	$\pm 0.135$	0.588	$\pm 0.151$	$\pm 0.045$	0.553	$\pm 0.139$	$\pm 0.023$
27.7–45.0	35.30	1.352	$\pm 0.442$	$\pm 0.218$	0.699	$\pm 0.280$	$\pm 0.056$	0.514	$\pm 0.202$	$\pm 0.060$

**Notes.** The columns indicate energy intervals  $E_1$ – $E_2$ , reference values  $\langle E \rangle$ , measured ratios, statistical errors, and systematic errors.

<sup>a</sup> The reference energy  $\langle E \rangle$  is computed as the geometric mean  $\sqrt{E_1 E_2}$ .

**Table 4**  
GALPROP Settings

Parameter	Name	Value
Diffusion—normalization	$D_0$	$5.85 \times 10^{28} \text{ cm}^2 \text{ s}^{-1}$
Diffusion—index	$\delta$	1/3
Reference rigidity	$R_0$	4 GV
Alfvén velocity	$V_a$	$30 \text{ km s}^{-1}$
Injection—index	$\alpha$	2.43
Halo height	$H$	4 kpc
Solar modulation	$\phi$	450 MV

## 6. CONCLUSIONS

We have presented a new measurement of light CR nuclei composition in the energy range from 0.35 to 45 GeV nucleon<sup>-1</sup> with the AMS-01 experiment. The isotopic ratio  ${}^7\text{Li}/{}^6\text{Li}$  has been measured between 2.5 and 6.3 GV of rigidity. This work is aimed at investigating the origin and the physical properties of the galactic CRs.

The study of highly charged ions with AMS-01 required the development of an improved charge identification algorithm. A thorough analysis has been made to understand the CR interactions in the spectrometer, its instrumental response, and the orbital environment. Our results for the B/C ratio agree well with the data collected from the HEAO-3-C2 experiment and with the more recent measurement from CREAM. The Li/C ratio has been measured with unprecedented accuracy. A 10%–15% overproduction of Be is found in the model predictions that well describe Li and B. This is consistent with the lack of cross section measurements that limits the model predictions up to uncertainties of  $\sim 20\%$  for light nuclei.

The astrophysical interest of light-nuclei CR flux measurements, both for propagation studies and in the search for exotic phenomenon, has been well established in the CR community. We expect, with AMS-02, to measure them with high precision over wide energy ranges in the near future.

The support of INFN, Italy, ETH-Zurich, the University of Geneva, the Chinese Academy of Sciences, Academia Sinica, and National Central University, Taiwan, the RWTH Aachen, Germany, the University of Turku, the University of Technology of Helsinki, Finland, the US DOE and MIT, CIEMAT, Spain, LIP, Portugal and IN2P3, France is gratefully acknowledged. The success of the first AMS mission is due to many individuals and organizations outside of the collaboration. The support of NASA was vital in the inception, development, and operation

of the experiment. Support from the Max-Planck Institute for Extraterrestrial Physics, from the space agencies of Germany (DLR), Italy (ASI), France (CNES), and China, and from CSIST, Taiwan played important roles in the success of AMS.

## REFERENCES

- Agostinelli, S., et al. 2003, *Nucl. Instrum. Methods A*, **506**, 250 (GEANT4)
- Aguilar, M., et al. 2002, *Phys. Rep.*, **366**, 331 (AMS-01)
- Aguilar, M., et al. 2005, *Nucl. Instrum. Methods B*, **234**, 321 (AMS-01)
- Ahlen, S. P., et al. 2000, *ApJ*, **534**, 757 (SMILI)
- Ahn, H. S., et al. 2008, *Astropart. Phys.*, **30**, 133 (CREAM)
- Ahn, H. S., et al. 2010, *ApJ*, **714**, L89 (CREAM)
- Asplund, M., Lambert, D. L., Nissen, P. E., Primas, F., & Smith, V. V. 2006, *ApJ*, **644**, 229
- Ave, M., Boyle, P. J., Höppner, C., Marshall, J., & Müller, D. 2009, *ApJ*, **697**, 106 (TRACER)
- Brun, R., et al. 1987, DD/EE/84-1 CERN (GEANT3)
- Buckley, J., Dwyer, J., Mueller, D., Swordy, S., & Tang, K. K. 1994, *ApJ*, **429**, 736
- Buffington, A., Orth, C. D., & Mast, T. S. 1978, *ApJ*, **226**, 335
- D’Agostini, G. 1995, *Nucl. Instrum. Methods A*, **362**, 487
- de Nolfo, G. A., et al. 2003, Proc. 28th ICRC (Tsukuba), 2, 1667 (CRIS)
- de Nolfo, G. A., et al. 2006, *Adv. Space Res.*, **38**, 1558
- Engelmann, J. J., Ferrando, P., Soutoul, A., Goret, P., & Juliusson, E. 1990, *A&A*, **233**, 96 (HEAO3-C2)
- Fassò, A., et al. 2005, CERN-2005-10, INFN/TC\_05/11, SLAC-R-773 (FLUKA)
- Fiandrini, E., et al. 2003, *J. Geophys. Res.*, **108**, A11
- Fiandrini, E., et al. 2004, *J. Geophys. Res.*, **109**, A10
- Gleeson, L. J., & Axford, W. I. 1968, *ApJ*, **154**, 1011
- Hams, T., et al. 2004, *ApJ*, **611**, 892 (ISOMAX)
- Hareyama, M., & Shibata, T. 2006, *J. Phys.*, **47**, 106 (RUNJOB)
- Hrivnacova, I., et al. 2003, Proc. CHEP La Jolla (CA); arXiv:astro-ph/0306005 (VMC)
- Lezniak, J. A., & Webber, W. R. 1978, *ApJ*, **223**, 676
- Maurin, D., Donato, F., Taillet, R., & Salati, P. 2001, *ApJ*, **555**, 585
- Moskalenko, I. V., & Mashnik, S. G. 2003, Proc. 28th ICRC (Tsukuba), 2, 1969
- Moskalenko, I. V., Strong, A. W., Ormes, J. F., & Potgieter, M. S. 2002, *ApJ*, **565**, 280
- Oliva, A. 2007, PhD Thesis, Univ. Perugia
- Orsi, S., et al. 2007, *Nucl. Instrum. Methods A*, **580**, 880 (PAMELA)
- Orth, C. D., Buffington, A., Smoot, G. F., & Mast, T. S. 1978, *ApJ*, **226**, 1147
- Panov, A. D., et al. 2007, Proc. 30th ICRC (Mérida), 2, 3 (ATIC)
- Reeves, H. 1994, *Rev. Mod. Phys.*, **66**, 193
- Salati, P., Donato, F., & Fornengo, N. 2010, in Particle Dark Matter—Observations, Models, and Searches, ed. G. Bertone (Cambridge: Cambridge Univ. Press), 521
- Simon, M., Spiegelhauer, H., Schmidt, W. K. H., Siohan, F., Ormes, J. F., Balasubrahmanyam, V. K., & Arens, J. F. 1980, *ApJ*, **239**, 712
- Smart, D. F., & Shea, M. A. 2005, *Adv. Space Res.*, **36**, 2012
- Sorge, H. 1995, *Phys. Rev. C*, **52**, 3291 (RQMD)
- Strong, A. W., & Moskalenko, I. V. 1998, *ApJ*, **509**, 212 (GALPROP)

- Strong, A. W., Moskalenko, I. V., & Ptuskin, V. S. 2007, *Annu. Rev. Nucl. Part. Sci.*, **57**, 285
- Sullivan, J. D. 1971, *Nucl. Instrum. Methods*, **95**, 5
- Swordy, S. P., Mueller, D., Meyer, P., L'Heureux, J., & Grunsfeld, J. M. 1990, *ApJ*, **349**, 625 (CRN)
- Tomassetti, N. 2009, PhD Thesis, Univ. Perugia
- Tomassetti, N., et al. 2009, Proc. 31st ICRC (Łódź), 1, 4 (AMS-01)
- Vangioni-Flam, E., Casséa, M., & Audouzea, J. 2000, *Phys. Rep.*, **333**, 365
- Webber, W. R., & Kish, J. 1979, Proc. 16th ICRC (Kyoto), 1, 389
- Webber, W. R., & Soutoul, A. 1998, *ApJ*, **506**, 335
- Webber, W. R., Damle, S. V., & Kish, J. 1972, *Astrophys. Space Sci.*, **15**, 245
- Webber, W. R., Lukasiak, A., & McDonald, F. B. 2002, *ApJ*, **568**, 210 (VOYAGER)
- Wiedenbeck, M. E., et al. 2007, Proc. 29th ICRC (Pune), 2, 277
- Zhou, F. 2009, PhD Thesis, Massachusetts Institute of Technology